Front. Optoelectron. 2020, 13(4): 307–317
https://doi.org/10.1007/s12200-020-1040-0

RESEARCH ARTICLE

In vivo volumetric monitoring of revascularization of traumatized skin using extended depth-of-field photoacoustic microscopy

Zhongwen CHENG[1], **Haigang MA**[2], **Zhiyang WANG**[2], **Sihua YANG** (✉)[1,2]

1 MOE Key Laboratory of Laser Life Science & Institute of Laser Life Science, College of Biophotonics,
South China Normal University, Guangzhou 510631, China
2 Guangdong Provincial Key Laboratory of Laser Life Science, College of Biophotonics,
South China Normal University, Guangzhou 510631, China

Abstract Faster and better wound healing is a critical medical issue. Because the repair process of wounds is closely related to revascularization, accurate early assessment and postoperative monitoring are very important for establishing an optimal treatment plan. Herein, we present an extended depth-of-field photoacoustic microscopy system (E-DOF-PAM) that can achieve a constant spatial resolution and relatively uniform excitation efficiency over a long axial range. The superior performance of the system was verified by phantom and *in vivo* experiments. Furthermore, the system was applied to the imaging of normal and trauma sites of volunteers, and the experimental results accurately revealed the morphological differences between the normal and traumatized skin of the epidermis and dermis. These results demonstrated that the E-DOF-PAM is a powerful tool for observing and understanding the pathophysiology of cutaneous wound healing.

Keywords photoacoustic microscopy (PAM), extended depth-of-field, traumatized skin

1 Introduction

Skin trauma occurs for many different reasons, including incisions, blunt force, and burns [1]. Chronic wounds, including diabetic, venous, and pressure ulcers, impose a significant healthcare burden worldwide [2]. Faster and better wound healing is a longstanding goal [3]. Accurate early assessment and postoperative monitoring are very important for establishing an appropriate treatment plan. Accurate early assessment can distinguish normal tissue from necrotic tissue, assist doctors in determining whether tissue removal and skin grafts are needed, and reduce waiting times [4]. The real-time postoperative monitoring of trauma sites can allow timely feedback of the effect of treatment and help doctors adjust treatment plans as soon as possible. Scars are the inevitable outcome of wound healing. Typically, visual observations and surface measurements have been used to evaluate wound healing by monitoring wound size, color, odor, drainage, and eschar [5]. However, such measurements are restricted to the skin's surface and depend heavily on the experience of medical professionals, the wound condition, and treatment history. Angiogenesis, the growth of new blood vessels from the existing host vasculature, plays an important role in the process of tissue repair [3]. New blood vessels support the delivery of nutrients and inflammatory cells to healing tissue, and its dynamic characteristics can reflect the situation of scar repair to a certain extent and can be used as an important indicator of scar monitoring [6]. Biopsies are the gold standard for scar detection, but they can cause secondary injury; thus, they are not widely used [7]. Meanwhile, various techniques have been developed to detect traumatized skin, such as fluorescence imaging, optical coherence tomography (OCT) imaging, ultrasonic imaging, laser Doppler perfusion imaging (LDI), and dynamic laser speckle imaging (LSI), but they have their own limitations. In fluorescence imaging, exogenous dyes, such as Evans blue and indocyanine green, are used to evaluate burn wounds [8–10]; however, the use of exogenous fuels may cause renal damage and allergic reactions. LDI and LSI can be used to evaluate vascular dysplasia in dermatosis without damage, but they cannot provide deep-resolved blood perfusion and blood flow

---

Received April 19, 2020; accepted May 27, 2020

E-mail: yangsh@scnu.edu.cn

information [11–13]. OCT, which is a promising method that visualizes photon scattering contrast in tissues, has been applied to measure the burn depth [14,15]. However, OCT lacks sensitivity to tissue chromophores, such as blood vessels with low blood flow or blood stasis. Ultrasonography has greater penetration depth but suffers from reduced contrast.

As a hybrid imaging technique, photoacoustic (PA) imaging (PAI) bridges the gap between optical and acoustic imaging modalities [16–20]. By offering high-resolution images with a unique optical contrast, optical resolution PA microscopy (OR-PAM), which is a unique implementation of PAI, has thus far been applied to numerous preclinical and human studies [21–27], including burn assessments [28]. However, the depth-of-field (DOF) of the conventional Gaussian beam PAM (GB-PAM) with a 4× objective is approximately 55 μm [29]. For wounds with a large area or uneven surface, imaging results are biased owing to the limited DOF. Recently, many methods have been proposed to improve the DOF. Hajireza et al. achieved wavelength-tuned depth scanning over more than 440 μm by using stimulated Raman scattering and chromatic aberration [30]. However, this method sacrifices the ability of functional imaging. Depth scanning by using a motor-driven linear platform or an electrically tunable lens can also improve the DOF [31,32]; however, these methods limit the volumetric imaging speed owing to the slow adjustment. Recently, a novel method was proposed to rapidly scan the optical focus along the depth direction in OR-PAM by employing a high-speed TAG lens [33,34] that can achieve a DOF of approximately 750 μm. However, this method requires additional external circuits, which increases the complexity of the system. As an alternative method, a non-diffracting Bessel beam can extend the DOF while preserving the high lateral resolution, and there are several ways to generate a Bessel beam. Among them, the use of an axicon lens is a typical method to extend the DOF, and many optical microscopy methods based on it have been reported [35–37]. However, it is difficult to produce an ideal conical surface, which will deform the Bessel beams [38]. Moreover, it usually requires a relay to further demagnify the initial Bessel beams produced by the axicon, which increases the complexity of the system. It has also been reported that a ring slit can be used to generate a Bessel beam [39]. However, the energy efficiency of this simple design is quite low. In some PAM systems, spatial light modulators are used to produce a Bessel beam [29,40]. The method can effectively improve the DOF but also increase the system complexity and cost, which is not conducive to clinical promotion. With the rapid development of etching technology and binary optical technology, the method of using refractive and diffractive optical elements to expand the focal depth provides the characteristics of free focus control, a high energy utilization rate, and uniform intensity distribution on the axis [38,41].

In this study, by utilizing a diffractive elongated focus (EF) lens to generate Bessel beams, we produced an extended DOF PAM (E-DOF-PAM) system that can achieve a relatively constant lateral resolution and uniform excitation efficiency at different depths without axial scanning. Furthermore, the E-DOF-PAM was applied to non-invasively explore the image characteristics related to pathophysiology of normal and traumatized skin.

2 Experimental methods

2.1 Experimental setup

A schematic of the E-DOF-PAM system is shown in Fig. 1(a). The system employs a 532-nm pulsed laser (Model DTL-314QT, Russia), which can operate at a repetition rate of up to 10 kHz. The laser beam is attenuated by a neutral density filter (NDF) and reshaped by an optical spatial filter system, which consists of a pair of lens, L1 and L2, and a pinhole. Then, the reshaped beam is coupled to a single-mode fiber (SMF) using a fiber coupler FC (PAF-X-7-A, Thorlabs, Inc., USA). The output laser beam from the SMF is collimated by a fiber collimator (F240FC-532, Thorlabs, Inc., USA) into a parallel one (~4-mm diameter). Then, the collimated beam passes through an 11-mm diameter EF lens (EF-027-Q-Y-A, HOLO/OR, Israel) with a focal length of ~25 mm to generate a Bessel beam, which is focused by a 4× objective lens. The DOF is proportional to the focal length of the focusing lens and inversely proportional to the collimated beam diameter. Additionally, the increase in the wavelength or refractive index of the medium also extends the DOF but at the cost of increasing the spot size [42]. The focused beam illuminates the sample surface through a hollow customized focused ultrasound transducer (7-mm outer diameter, 3-mm inner diameter, and central frequency of 40 MHz) and performs a raster-scanning pattern using a two dimensional scanner (HRXWJ-50R-2, TianRui ZhongHai, China). Figure 1(b) illustrates the optical path of the GB-PAM system. Notably, a Bessel beam can be generated by adding an EF lens to the optical path of the GB-PAM without significant changes in the optical setup. The numerical simulation intensity distributions of the laser beams generated with and without the EF lens along the optical axis at the focal zone are presented in Figs. 2(a) and 2(c), respectively. As expected, the Bessel beam has a longer DOF. Figures 2(b) and 2(d) show the corresponding laser beam intensity maps indicated by dashed lines A-A' and B-B' in Figs. 2(a) and 2(c), respectively.

2.2 Data acquisition and processing

The detected PA signals were amplified by a 50-dB low-noise amplifier (LNA-650, RFBAY, USA) and then

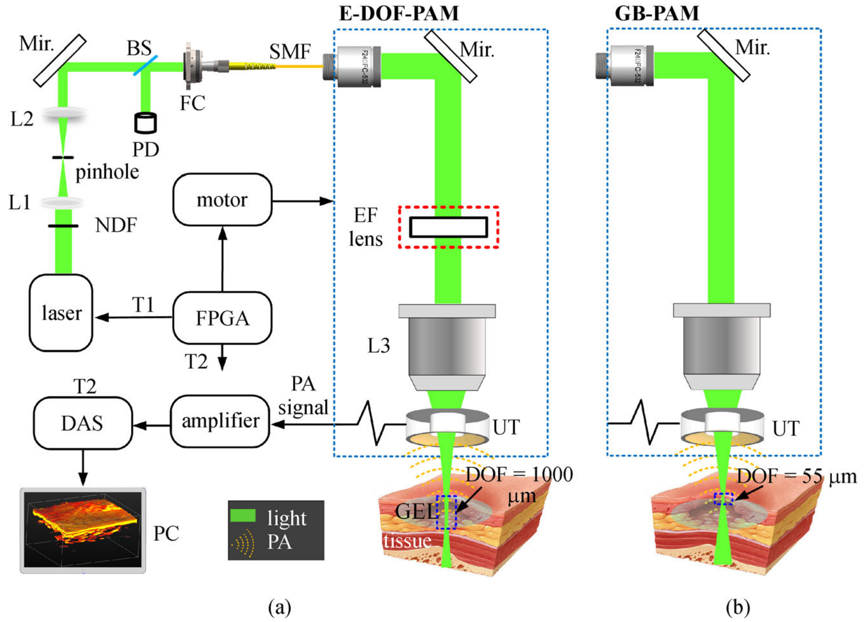

Fig. 1 Schematic illustration of the E-DOF-PAM (with an EF lens) and conventional GB-PAM (without an EF lens) systems. (a) Schematic of the E-DOF-PAM system. (b) Optical path of the GB-PAM system. E-DOF-PAM, extended depth-of-field photoacoustic microscopy; GB-PAM, Gaussian beam photoacoustic microscopy; L1, L2, L3, lenses; Mir., mirror; SMF, single-mode fiber; EF, elongated focus; NDF, neutral density filter; PD, photodiode; T1, T2, trigger; DAS, data acquisition system; FPGA, field programmable gate array; WT, water; UT, ultrasound transducer

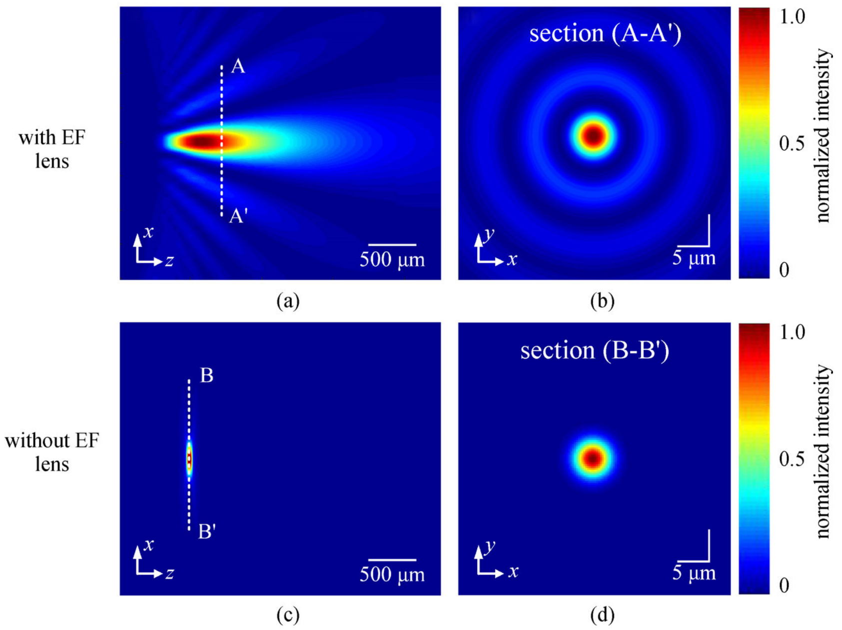

Fig. 2 Numerical simulation intensity distributions of the laser beams generated with and without elongated focus (EF) lenses in the *x*-*z* and *x*-*y* planes. (a) Calculated intensity distribution of the Bessel beam (with EF lens) along the *z* axis (optical axis) at the focal zone. (b) Corresponding laser beam intensity maps indicated by the dashed line A-A' in (a). (c) Calculated intensity distribution of the Gaussian beam (without EF lens) along the *z* axis. (d) Corresponding laser beam intensity maps indicated by the dashed line B-B' in (c)

collected by a data acquisition card (M3i.4121, SPECTRUM, Germany) at a sampling rate of 200 MHz. All PA data were collected and processed by user-defined LabVIEW (National Instruments, Inc., USA) and MATLAB (R2016a, MathWorks, Natick, MA, USA) programs on a PC with an Intel(R) Core(TM) i7 CPU @4.0 GHz and 32 GB of RAM. The PA data were averaged 10 times during the *in vivo* experiments. To suppress the artifacts introduced by the side lobes of the Bessel beam, a blind deconvolution operation proposed in a previous study was adopted [35].

The PA intensity in the region of interest (ROI) was analyzed by using ImageJ software. In addition, ImageJ was used to measure the thickness of the skin epidermis and the diameters of the blood vessels.

2.3 Phantom studies

Performance of the E-DOF-PAM system was first verified via phantom studies. For the purpose of assessing the lateral and axial resolutions, two phantom experiments were conducted. In the first experiment, a surgical blade was obliquely inserted into a tissue-mimicking background phantom [43,44]. The experiment was quantified by imaging the sharp surgical blade with a scanning step of 1 μm. In the second experiment, the pulse response of the detector at the focus was measured, and the signal was transformed using the Hilbert method to test the axial resolution. Following previous studies [45,46], the axial resolution was taken as the full width at half-maximum (FWHM) of the Hilbert-transformed envelope. Additionally, to verify the depth imaging performance of the system, an experiment involving two human hairs was performed using the E-DOF-PAM and GB-PAM systems. The beams were set to the same input power, and each focus was located on the surface of the sample in the two systems.

2.4 *In vivo* human experiments

To demonstrate the clinical potential of the E-DOF-PAM system, two volunteers from the authors were recruited for experiments. Normal skin and traumatized skin of the human subjects were imaged *in vivo*. To conform to the American National Standards Institute safety limit (20 mJ/cm^2), the NDF was used to adjust the fluence density of the laser beam on the tissue surface to 15 mJ/cm^2. During the experiment, the volunteers sat in chairs and wore goggles to avoid potential laser damage. After the experiment, the clinician examined the imaged area, and no obvious damage was found. The consents of the volunteers were obtained prior to the experiments, and all procedures were approved by South China Normal University in Guangzhou, China.

3 Results

3.1 Resolution characterization

For the PAM system, the field characteristic of the built transducer is a critical factor that determines the accuracy of the image reconstruction. Figure 3(a) shows the measured acoustic pressure distribution of the transducer. The acoustic field was well focused, and the focal length was approximately 8 mm. The DOF of the transducer was approximately 3.8 mm. Figure 3(b) depicts the pulse response of the transducer at the focus (black line), and the red dashed line is the corresponding Hilbert-transformed envelope. The axial resolution was measured to be approximately 35 μm. The amplitude–frequency response of the transducer is shown in Fig. 3(c). Based on the amplitude–frequency response, the central frequency and bandwidth of the transducer were estimated to be 40 MHz and 120%, respectively. To evaluate the lateral resolution, the fitted edge spread function (ESF) was estimated from the blade's PA data along the white dashed line shown in Fig. 3(e). The line spread function (LSF) was calculated as the derivative of the ESF, and the FWHM of the LSF was defined as the lateral resolution. As shown in Fig. 3(d), the lateral resolution of the E-DOF-PAM was slightly worse than that of the GB-PAM system (6.5 μm vs. 4.7 μm, respectively). The deconvolution operation may degrade the effective resolution. Figure 3(f) illustrates the variation of the experimentally measured lateral resolution along the optical axis of the E-DOF-PAM and GB-PAM. The lateral resolution of the E-DOF-PAM changed slightly, whereas that of the GB-PAM varied dramatically as it moved away from the focus. The DOF of the E-DOF-PAM was found to be approximately 1.0 mm, which was much longer than that of the GB-PAM.

3.2 Verification of depth imaging performance

To demonstrate the depth imaging performance of the E-DOF-PAM, a phantom study was performed. A 3D schematic illustration of the phantom is shown in Fig. 4(a). Two human hairs were embedded in a tissue-mimicking background phantom. One was placed horizontally, and the other was inserted obliquely; additionally, the vertical drop of the two hairs ranged from 0 to 1.0 mm. Figures 4(b) and 4(c) show the maximum amplitude projection (MAP) PA images acquired by the two systems, respectively. As expected, E-DOF-PAM exhibited a consistent PA intensity throughout the entire depth, whereas the intensity of the PA image acquired by GB-PAM showed significant differences. Moreover, the line profiles, as indicated by dashed lines 1 and 2 in Figs. 4(b) and 4(c), across the human hairs at different depths were taken to quantitatively compare the signal amplitudes, and the results are shown in Figs. 4(d) and 4(e). Apparently,

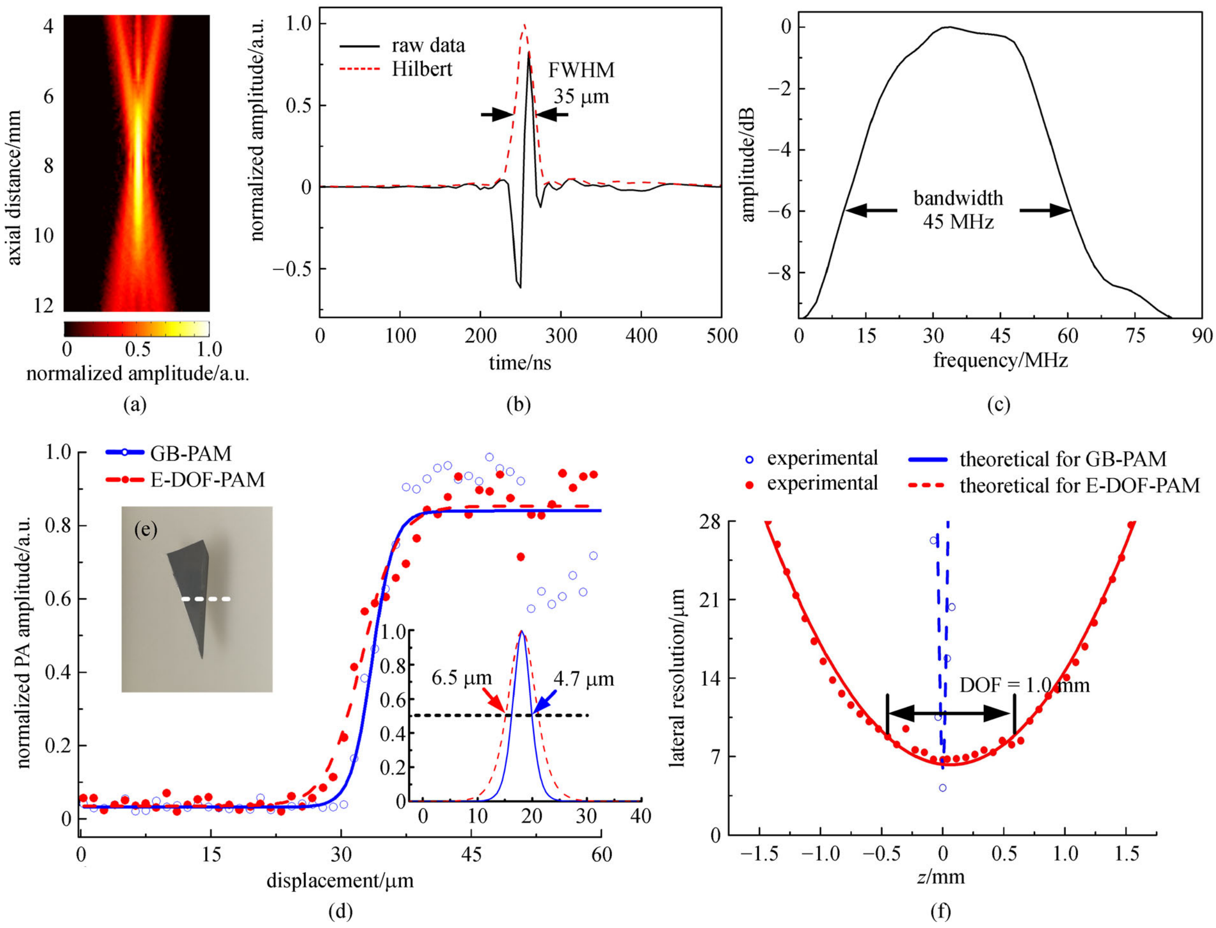

Fig. 3 Performance of the E-DOF-PAM system. (a) Acoustic pressure distribution of the transducer. (b) Pulse response of the detector at the focus. (c) Amplitude–frequency response of the detector. (d) Edge spread function (ESF) extracted from (e) along the dashed line and the line spread function (LSF) obtained by taking the derivative of the ESF by the conventional GB-PAM (without an EF lens) and E-DOF-PAM (with an EF lens) systems, respectively. (e) Photo of a sharp-edged surgical blade. (f) Lateral resolution of the GB-PAM and E-DOF-PAM systems vs. the depth along the z axis

toward the ends of the depth range, the PA signal amplitudes were more resolvable in the E-DOF-PAM than in the GB-PAM. Moreover, a variation graph of the normalized PA signal amplitudes vs. the depth from Figs. 4(b) and 4(c) is shown in Fig. 4(f). Owing to the severe degradation of Gaussian beams out of focus, the PA amplitude acquired by GB-PAM reduced to half when the depth was 0.3 mm. However, when the depth was 1 mm, the PA amplitude of E-DOF-PAM was still as high as 0.6. Overall, the results demonstrated that E-DOF-PAM has a better depth imaging performance.

3.2.1 *In vivo* imaging of normal skin

To verify the *in vivo* imaging ability of the GB-PAM and E-DOF-PAM systems on uneven tissue, an area in the middle finger of a healthy volunteer’s opisthenar was chosen for PA imaging; the imaged area was 5 mm × 4 mm. The speed of the fast axis motor was set to 10 mm/s, which means that the step size of the x axis was 10 μm over an average of 10 times, and the step size of the y axis was also set to 10 μm to ensure equidistant sampling. The MAP images acquired by the GB-PAM and E-DOF-PAM systems are presented in Figs. 5(a) and 5(b), respectively. Owing to the limited DOF, the PA image acquired by the GB-PAM system (Fig. 5(a)) shows a significant fluctuation in PA intensity over the scanning range. However, the image acquired by the E-DOF-PAM system (Fig. 5(b)) reveals uniform PA intensity over a long depth range. Figures 5(c) and 5(d) show PA cross-sectional images corresponding to the dashed lines A-A' and B-B' in Figs. 5(a) and 5(b), respectively. As shown, the stratum corneum (SC) and stratum basale (SB) layers in the epidermis are clearly visible in Figs. 5(c) and 5(d); however, the PA intensity of the SB and SC at the focus is much stronger than that of the defocus in Fig. 5(c). Figures 5(e) and 5(g)

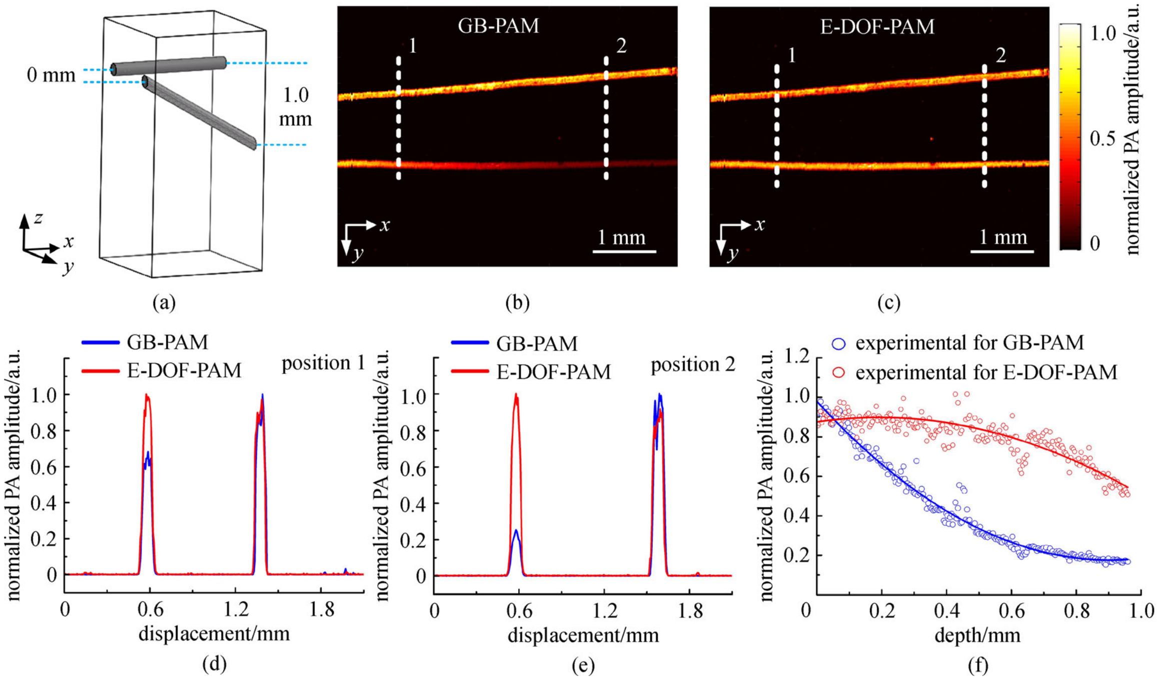

Fig. 4 PA image of human hairs acquired by the E-DOF-PAM and GB-PAM systems. (a) 3D schematic diagram of the phantom. (b) and (c) Maximum amplitude projection (MAP) PA images acquired by the E-DOF-PAM and GB-PAM systems, respectively. (d) and (e) Corresponding line profiles at positions indicated by dashed lines 1 and 2 are shown in (b) and (c). (f) Normalized PA amplitude versus the depth for the two systems

show the corresponding B-scan images at positions I and II in Fig. 5(c), and Figs. 5(f) and 5(h) show the B-scan images corresponding to positions III and IV in Fig. 5(d), respectively. Obviously, owing to the tight light focus, there are many blood vessels beneath the epidermis shown in the B-scan image at position I, whereas the epidermis for the B-scan at position II can be hardly distinguished because of the reduction in the light excitation energy. However, as shown in Figs. 5(f) and 5(h), there is no significant difference in the PA images at positions III and IV, and both show a large number of blood vessels under the epidermal layer. The corresponding PA amplitude profiles along the dashed lines at positions I–IV in Figs. 5(c) and 5(d) are presented in Figs. 5(i) and 5(j), respectively. Thus, for the same depth range (~500 μm), the amplitude of the corresponding PA signal at positon I is approximately 2.8 times that at position II, whereas the amplitudes of the signals at positions III and IV are almost the same. Therefore, we concluded that E-DOF-PAM is superior to GB-PAM when imaging tissue with an uneven surface, which is more suitable for *in vivo* quantitative measurement and imaging over a large area.

3.2.2 *In vivo* imaging of traumatized skin

To further demonstrate the clinical feasibility of monitoring the revascularization of traumatized skin, normal and trauma sites of another volunteer were imaged and quantitatively analyzed by the E-DOF-PAM system. Figure 6(a) shows a photograph of the volunteer's opisthenar, where the sites of normal skin (enclosed by black dashed box I) and traumatized skin (enclosed by white dashed box II) were chosen for PA imaging (imaging area was approximately 5 mm × 4 mm). Through visual inspection, the trauma site, which was caused by a burn, was dark red. Figures 6(b) and 6(c) show the corresponding PA MAP images. As shown in Fig. 6(c), there was a clear boundary between the normal and trauma sites, and the morphological features of the traumatized skin were quite different from those of normal skin. Figures 6(d) and 6(e) show the B-scan images marked by white dashed lines A-A' and B-B' in Fig. 6(c), respectively. According to simple observation, the epidermis of normal skin has continuous SC and SB layers, and the PA intensity of the SB layer is significantly higher than that of the SC layer, which is mainly because that there are many melanosomes in the SB layer [47]. However, in Fig. 6(d), the SB layer disappeared, and the intensity of the SC layer was higher than that of normal skin. This may be due to destruction of cells in the SB layer. To more intuitively observe the changes in different layers of traumatized skin, volumetric (3D) PA images of the trauma site at different depths were generated. For this, an automatic segmentation algorithm [41] was used to segment the 3D images into depth-resolved physiologic layers. The generated three layers were the SC layer, SB layer, and vascular network layer,

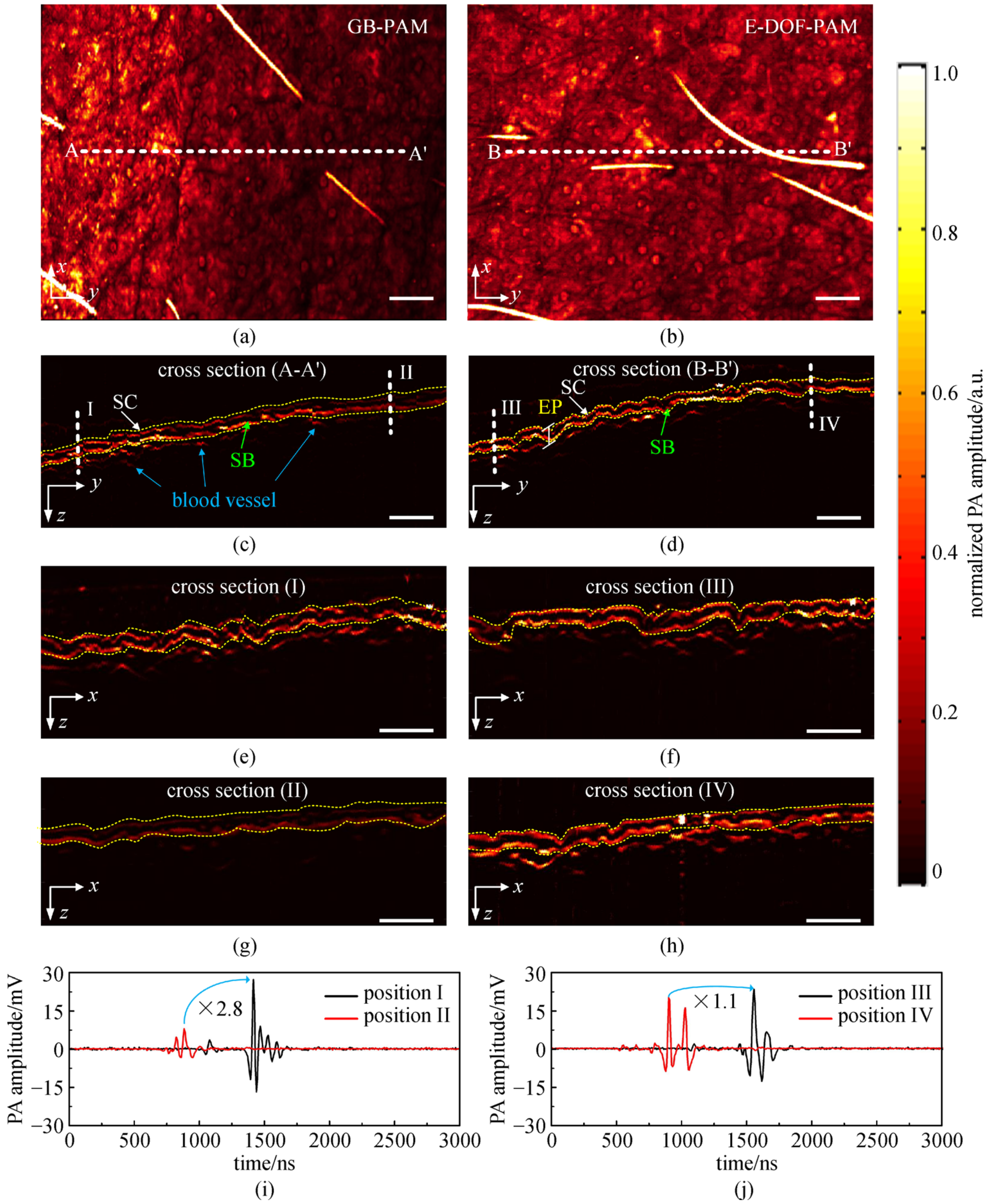

Fig. 5 Verification of *in vivo* imaging abilities of the GB-PAM and E-DOF-PAM systems on uneven tissue in the middle finger of a volunteer. (a) and (b) MAP PA images acquired by the GB-PAM and E-DOF-PAM systems, respectively. (c) and (d) PA cross-sectional images along the dashed lines A-A' and B-B' in (a) and (b), respectively. (e) and (g) Corresponding PA cross-sectional images along the dashed lines at positons I and II in (c), respectively. (f) and (h) Corresponding PA cross-sectional images along the dashed lines at positons III and IV in (d), respectively. (i) and (j) Corresponding PA amplitude profiles along the dashed lines at positions I–IV in (c) and (d), respectively. EP, epidermis; SC, stratum corneum layer; SB, stratum basale. Scalar bar, 500 μm

which are shown in Figs. 6(f)–6(h), respectively. In the SC layer (Fig. 6(f)), the trauma site was irregular and completely different from that of the normal site. According to ROIs 3 and 4 in Fig. 6(g), the SB layer at the trauma site was severely damaged and replaced with a large number of capillaries, which may be the reason why the trauma site was darker than the normal site. Figure 6(h) shows the vascular network beneath the epidermis. Obviously, the blood vessels in the trauma site were very different in morphology and diameter from the blood vessels in the normal site. The microvasculature at the trauma site was small and dense. Figure 6(i) shows a statistical analysis of the thickness and normalized PA amplitude of the SC layers for the normal and trauma sites. The SC's thickness and PA amplitude of the traumatized skin were 1.58 times and 3.57 times that of the normal skin, respectively. The thickness of the SC layer was measured from Figs. 6(d) and 6(e), and the normalized PA

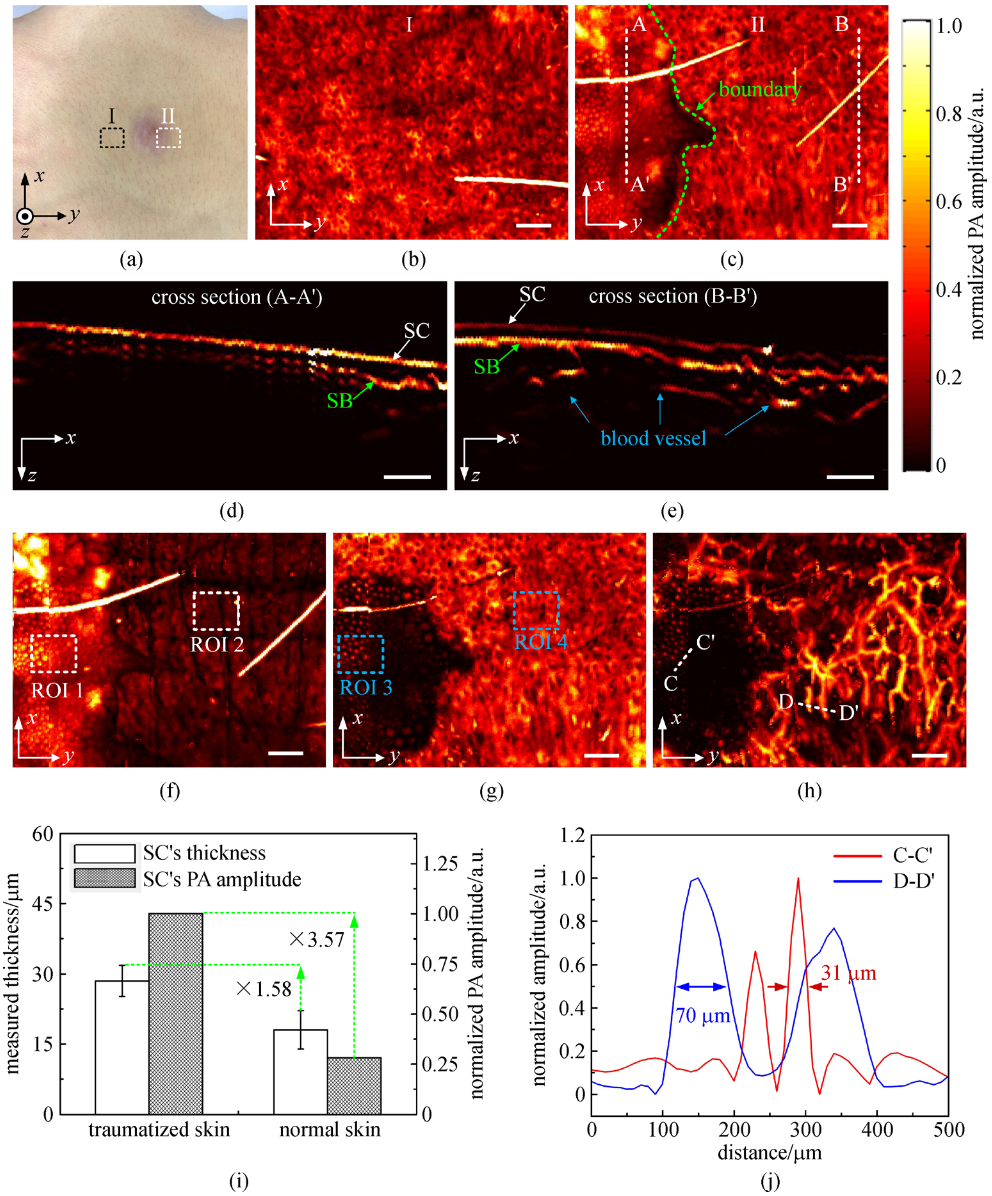

Fig. 6 Feasibility of the E-DOF-PAM system in the detection of uneven traumatized skin. (a) Photograph of another volunteer's skin, where the normal and trauma sites, which are enclosed by dashed black and white boxes, were chosen for PA imaging. (b) and (c) MAP PA images corresponding to the normal and trauma sites. (d) and (e) PA cross-sectional images along dashed lines A-A' and B-B' in (c), respectively. (f)–(h) MAP PA images of the SC layer, SB layer, and vascular network beneath the epidermis, respectively. (i) Statistical analysis of the measured thickness and normalized PA amplitude of the SC of the normal and traumatized skin. (j) Corresponding line profiles along the lines C-C' and D-D' in (h). SC, stratum corneum; SB, stratum basale; ROI, region of interest. Scalar bar, 500 μm

amplitudes were obtained from ROIs 1 and 2 in Fig. 6(f). To compare the diameters of the blood vessels in the normal and trauma sites, the profiles traced along lines C-C' and D-D' in Fig. 6(h) are shown in Fig. 6(j). Obviously, the diameters of the blood vessel at the trauma site were smaller than those at the normal site. These results show that E-DOF-PAM has the ability to reveal the morphological changes of traumatized skin, and it can be used to monitor the revascularization of traumatized skin.

4 Discussion and conclusions

We developed an E-DOF-PAM system by using an EF lens to generate a non-diffracting Bessel beam, which can achieve a DOF of up to 1000 μm and have a relative uniform excitation efficiency at the focus. Meanwhile, scattering phantoms and *in vivo* human skin experiments demonstrated that the E-DOF-PAM has superior capacity to image uneven tissues with high resolution and a large

DOF. Furthermore, E-DOF-PAM was used to image traumatized skin, and the volumetric PA images clearly revealed detailed information about the epidermal structure and neovascularization. The morphological differences between normal skin and traumatized skin demonstrate the feasibility of E-DOF-PAM in monitoring skin trauma and regeneration, helping clinicians to quantitatively access the treatment outcome. However, there are still some limitations. Primarily, the cohort recruited here would not be sufficient for a more comprehensive clinical investigation, and only the feasibility of the E-DOF-PAM system for monitoring traumatized skin is demonstrated in this study. Additionally, the contact measurement limits the clinical settings to some extent. The system can be further developed to provide pathophysiological information in a noncontact fashion, such as by being equipped with a high-frequency air-coupled ultrasonic transducer or by using an all-optical detection method [28,48]. Finally, to obtain a greater imaging depth, a longer wavelength irradiation source may be needed. Moreover, a multi-wavelength application should be added to the system, which would enable the system to measure oxyhemoglobin saturation.

Acknowledgements This work was supported by the National Natural Science Foundation of China (Grant Nos. 61822505, 11774101, 61627827, and 81630046), the Science and Technology Planning Project of Guangdong Province, China (No. 2015B020233016), and the Science and Technology Program of Guangzhou (No. 2019050001).

References

1. Valvis S M, Waithman J, Wood F M, Fear M W, Fear V S. The immune response to skin trauma is dependent on the etiology of injury in a mouse model of burn and excision. Journal of Investigative Dermatology, 2015, 135(8): 2119–2128
2. Qin W, Li Y, Wang J, Qi X, Wang R K. *In vivo* monitoring of microcirculation in burn healing process with optical microangiography. Advances in Wound Care, 2016, 5(8): 332–337
3. Wang H, Shi L, Qin J, Yousefi S, Li Y, Wang R K. Multimodal optical imaging can reveal changes in microcirculation and tissue oxygenation during skin wound healing. Lasers in Surgery and Medicine, 2014, 46(6): 470–478
4. Hoeksema H, Van de Sijpe K, Tondu T, Hamdi M, Van Landuyt K, Blondeel P, Monstrey S. Accuracy of early burn depth assessment by laser Doppler imaging on different days post burn. Burns, 2009, 35(1): 36–45
5. Deegan A J, Wang W, Men S, Li Y, Song S, Xu J, Wang R K. Optical coherence tomography angiography monitors human cutaneous wound healing over time. Quantitative Imaging in Medicine and Surgery, 2018, 8(2): 135–150
6. Kumar I, Staton C A, Cross S S, Reed M W, Brown N J. Angiogenesis, vascular endothelial growth factor and its receptors in human surgical wounds. British Journal of Surgery, 2009, 96(12): 1484–1491
7. Wang N, Wei H, Jin Y, Chen L, Zhang Q, Deng X. Monitoring skin trauma healing in mice using second-harmonic generation combined with optical coherence tomography. IEEE Photonics Journal, 2017, 9(4): 1–12
8. Atiyeh B S, Gunn S W, Hayek S N. State of the art in burn treatment. World Journal of Surgery, 2005, 29(2): 131–148
9. Still J M, Law E J, Klavuhn K G, Island T C, Holtz J Z. Diagnosis of burn depth using laser-induced indocyanine green fluorescence: a preliminary clinical trial. Burns, 2001, 27(4): 364–371
10. McUmber H, Dabek R J, Bojovic B, Driscoll D N. Burn depth analysis using indocyanine green fluorescence: a review. Journal of Burn Care & Research, 2019, 40(4): 513–516
11. Qin J, Jiang J, An L, Gareau D, Wang R K. *In vivo* volumetric imaging of microcirculation within human skin under psoriatic conditions using optical microangiography. Lasers in Surgery and Medicine, 2011, 43(2): 122–129
12. Burke-Smith A, Collier J, Jones I. A comparison of non-invasive imaging modalities: infrared thermography, spectrophotometric intracutaneous analysis and laser Doppler imaging for the assessment of adult burns. Burns, 2015, 41(8): 1695–1707
13. Pape S A, Skouras C A, Byrne P O. An audit of the use of laser Doppler imaging (LDI) in the assessment of burns of intermediate depth. Burns, 2001, 27(3): 233–239
14. Pierce M C, Sheridan R L, Hyle Park B, Cense B, de Boer J F. Collagen denaturation can be quantified in burned human skin using polarization-sensitive optical coherence tomography. Burns, 2004, 30(6): 511–517
15. Jiao S, Yu W, Stoica G, Wang L V. Contrast mechanisms in polarization-sensitive Mueller-matrix optical coherence tomography and application in burn imaging. Applied Optics, 2003, 42(25): 5191–5197
16. Schwarz M, Soliman D, Omar M, Buehler A, Ovsepian S V, Aguirre J, Ntziachristos V. Optoacoustic dermoscopy of the human skin: tuning excitation energy for optimal detection bandwidth with fast and deep imaging *in vivo*. IEEE Transactions on Medical Imaging, 2017, 36(6): 1287–1296
17. Liu W, Yao J. Photoacoustic microscopy: principles and biomedical applications. Biomedical Engineering Letters, 2018, 8(2): 203–213
18. Yao J, Wang L, Yang J M, Maslov K I, Wong T T, Li L, Huang C H, Zou J, Wang L V. High-speed label-free functional photoacoustic microscopy of mouse brain in action. Nature Methods, 2015, 12(5): 407–410
19. Yang J, Zhang G, Wu M, Shang Q, Huang L, Jiang H. Photoacoustic assessment of hemodynamic changes in foot vessels. Journal of Biophotonics, 2019, 12(6): e201900004
20. Ma H, Cheng Z, Wang Z, Xiong K, Yang S. Fast controllable confocal focus photoacoustic microscopy using a synchronous zoom opto-sono objective. Optics Letters, 2019, 44(7): 1880–1883
21. Xu D, Yang S, Wang Y, Gu Y, Xing D. Noninvasive and high-resolving photoacoustic dermoscopy of human skin. Biomedical Optics Express, 2016, 7(6): 2095–2102
22. Zhou W, Hu Y, Chen Z, Xing D. All-optical photoacoustic and reflectance confocal microscopy for melanoma characterization. Applied Physics Letters, 2019, 114(16): 163704
23. Ma H, Cheng Z, Wang Z, Gu Y, Zhang T, Qiu H, Yang S. Fast linear confocal scanning photoacoustic dermoscopy for non-invasive assessment of chromatodermatosis. Applied Physics Letters, 2018,

113(8): 083704

24. Li X, Dinish U S, Aguirre J, Bi R, Dev K, Attia A B E, Nitkunanantharajah S, Lim Q H, Schwarz M, Yew Y W, Thng S T G, Ntziachristos V, Olivo M. Optoacoustic mesoscopy analysis and quantitative estimation of specific imaging metrics in Fitzpatrick skin phototypes II to V. Journal of Biophotonics, 2019, 12(9): e201800442
25. Aguirre J, Schwarz M, Garzorz N, Omar M, Buehler A, Kilian Eyerich K, Ntziachristos V. Precision assessment of label-free psoriasis biomarkers with ultra-broadband optoacoustic mesoscopy. Nature Biomedical Engineering, 2017, 1(5): 0068
26. Zhang W, Li Y, Nguyen V P, Huang Z, Liu Z, Wang X, Paulus Y M. High-resolution, *in vivo* multimodal photoacoustic microscopy, optical coherence tomography, and fluorescence microscopy imaging of rabbit retinal neovascularization. Light, Science & Applications, 2018, 7(1): 103
27. Tian C, Zhang W, Mordovanakis A, Wang X, Paulus Y M. Noninvasive chorioretinal imaging in living rabbits using integrated photoacoustic microscopy and optical coherence tomography. Optics Express, 2017, 25(14): 15947–15955
28. Ma H, Xiong K, Wu J, Ji X, Yang S. Noncontact photoacoustic angiography with an air-coupled ultrasonic transducer for evaluation of burn injury. Applied Physics Letters, 2019, 114(13): 133701
29. Yang J, Gong L, Xu X, Hai P, Shen Y, Suzuki Y, Wang L V. Motionless volumetric photoacoustic microscopy with spatially invariant resolution. Nature Communications, 2017, 8(1): 780
30. Hajireza P, Forbrich A, Zemp R J. Multifocus optical-resolution photoacoustic microscopy using stimulated Raman scattering and chromatic aberration. Optics Letters, 2013, 38(15): 2711–2713
31. Li B, Qin H, Yang S, Xing D. *In vivo* fast variable focus photoacoustic microscopy using an electrically tunable lens. Optics Express, 2014, 22(17): 20130–20137
32. Yeh C, Soetikno B, Hu S, Maslov K I, Wang L V. Microvascular quantification based on contour-scanning photoacoustic microscopy. Journal of Biomedical Optics, 2014, 19(9): 096011
33. Yang X, Jiang B, Song X, Wei J, Luo Q. Fast axial-scanning photoacoustic microscopy using tunable acoustic gradient lens. Optics Express, 2017, 25(7): 7349–7357
34. Yang X, Song X, Jiang B, Luo Q. Multifocus optical-resolution photoacoustic microscope using ultrafast axial scanning of single laser pulse. Optics Express, 2017, 25(23): 28192–28200
35. Jiang B, Yang X, Luo Q. Reflection-mode Bessel-beam photoacoustic microscopy for *in vivo* imaging of cerebral capillaries. Optics Express, 2016, 24(18): 20167–20176
36. Chen B, Huang X, Gou D, Zeng J, Chen G, Pang M, Hu Y, Zhao Z, Zhang Y, Zhou Z, Wu H, Cheng H, Zhang Z, Xu C, Li Y, Chen L, Wang A. Rapid volumetric imaging with Bessel-beam three-photon microscopy. Biomedical Optics Express, 2018, 9(4): 1992–2000
37. Shi J, Wang L, Noordam C, Wang L V. Bessel-beam Grueneisen relaxation photoacoustic microscopy with extended depth of field. Journal of Biomedical Optics, 2015, 20(11): 116002
38. Liu Z, Fulop G F, Flores A, Wang M R, Yang J J. Infrared imaging lens with extended depth of focus. In: Proceedings of SPIE Infrared Technology and Applications XXXI. Bellingham: SPIE, 2005, 841–848
39. Durnin J, Miceli J Jr, Eberly J H. Diffraction-free beams. Physical Review Letters, 1987, 58(15): 1499–1501
40. Song W, Wu Y, Gao Y, Chen T, Zheng W, Fang H, Song L, Yuan X. Flexibly adjustable depth-of-focus photoacoustic microscopy with spatial light modulation. Applied Physics Letters, 2018, 113(16): 163502
41. Flores A, Wang M R, Yang J J. Achromatic hybrid refractive-diffractive lens with extended depth of focus. Applied Optics, 2004, 43(30): 5618–5630
42. Li X, Xiong K, Yang S. Large-depth-of-field optical-resolution colorectal photoacoustic endoscope. Applied Physics Letters, 2019, 114(16): 163703
43. Cheng Z, Ma H, Wang Z, Yang S. 3D depth-coded photoacoustic microscopy with a large field of view for human skin imaging. Chinese Optics Letters, 2018, 16(8): 081701
44. Zhang W, Ma H, Cheng Z, Wang Z, Zhang L, Yang S. Miniaturized photoacoustic probe for *in vivo* imaging of subcutaneous microvessels within human skin. Quantitative Imaging in Medicine and Surgery, 2019, 9(5): 807–814
45. Chen Q, Guo H, Jin T, Qi W, Xie H, Xi L. Ultracompact high-resolution photoacoustic microscopy. Optics Letters, 2018, 43(7): 1615–1618
46. Wang H, Yang X, Liu Y, Jiang B, Luo Q. Reflection-mode optical-resolution photoacoustic microscopy based on a reflective objective. Optics Express, 2013, 21(20): 24210–24218
47. Matts P J, Dykes P J, Marks R. The distribution of melanin in skin determined *in vivo*. British Journal of Dermatology, 2007, 156(4): 620–628
48. Hu Y, Chen Z, Xiang L, Xing D. Extended depth-of-field all-optical photoacoustic microscopy with a dual non-diffracting Bessel beam. Optics Letters, 2019, 44(7): 1634–1637

Zhongwen Cheng is a Ph.D. candidate student from College of Biophotonics, South China Normal University, China. His research interests includes photoacoustic microscopy and photoacoustic tomography.

Haigang Ma is a Ph.D. candidate student from College of Biophotonics, South China Normal University, China. His research interests includes utilizing photoacoustic imaging for detection of skin diseases and clinical applications.

Zhiyang Wang is a Ph.D. candidate student from College of Biophotonics, South China Normal University, China. His research interests focus on photoacoustic microscopy and its clinical applications.

Sihua Yang is a professor at MOE Key Laboratory of Laser Life Science & Institute of Laser Life Science, College of Biophotonics, South China Normal University, China. His research focuses on photoacoustic imaging, photoacoustic endoscopic technology, instrumentation and their biomedical applications.